

# Molecular Gas in Infrared Ultraluminous QSO Hosts

X.Y. Xia<sup>1</sup>, Y. Gao<sup>2,3</sup>, C.-N. Hao<sup>1</sup>, Q. H. Tan<sup>2,3,4</sup>, S. Mao<sup>5,6</sup>, A. Omont<sup>7</sup>, B. O. Flaquer<sup>8</sup>, S. Leon<sup>8,9</sup>, P. Cox<sup>10</sup>

## ABSTRACT

We report CO detections in 17 out of 19 infrared ultraluminous QSO (IR QSO) hosts observed with the IRAM 30m telescope. The cold molecular gas reservoir in these objects is in a range of  $0.2\text{--}2.1 \times 10^{10} M_{\odot}$  (adopting a CO-to-H<sub>2</sub> conversion factor  $\alpha_{\text{CO}} = 0.8 M_{\odot} (\text{K km s}^{-1} \text{ pc}^2)^{-1}$ ). We find that the molecular gas properties of IR QSOs, such as the molecular gas mass, star formation efficiency ( $L_{\text{FIR}}/L'_{\text{CO}}$ ) and the CO (1-0) line widths, are indistinguishable from those of local ultraluminous infrared galaxies (ULIRGs). A comparison of low- and high-redshift CO detected QSOs reveals a tight correlation between  $L_{\text{FIR}}$  and  $L'_{\text{CO}(1-0)}$  for all QSOs. This suggests that, similar to ULIRGs, the far-infrared emissions of all QSOs are mainly from dust heated by star formation rather than by active galactic nuclei (AGNs), confirming similar findings from mid-infrared spectroscopic observations by *Spitzer*. A correlation between the AGN-associated bolometric luminosities and the CO line luminosities suggests that star formation

---

<sup>1</sup>Tianjin Astrophysics Center, Tianjin Normal University, Tianjin 300387, China; xyxia@bao.ac.cn

<sup>2</sup>Purple Mountain Observatory, Chinese Academy of Sciences, 2 West Beijing Road, Nanjing 210008, China

<sup>3</sup>Key Laboratory of Radio Astronomy, Chinese Academy of Sciences, Nanjing 210008, China

<sup>4</sup>Graduate School of Chinese Academy of Sciences, Beijing 100039, China

<sup>5</sup>National Astronomical Observatories of China, 20A Datun Road, Chaoyang District, Beijing 100012, China

<sup>6</sup>Jodrell Bank Centre for Astrophysics, University of Manchester, Alan Turing Building, Manchester M13 9PL, UK

<sup>7</sup>Institut d'Astrophysique de Paris, UMR7095, UPMC and CNRS, 98bis boulevard Arago, F-75014, Paris, France

<sup>8</sup>Instituto de Radioastronomía Milimétrica (IRAM), Avenida Divina Pastora 7, Núcleo Central, 18012 Granada, Spain

<sup>9</sup>Joint Alma Observatory/ESO, Av. El Golf 40, Piso 18, Las Condes, Santiago, Chile

<sup>10</sup>Institut de Radio Astronomie Millimetrique (IRAM), St. Martin d'Herès, France

and AGNs draw from the same reservoir of gas and there is a link between star formation on  $\sim$  kpc scale and the central black hole accretion process on much smaller scales.

*Subject headings:* galaxies: active — galaxies: evolution — galaxies: high-redshift — galaxies: starburst — radio lines: galaxies

## 1. INTRODUCTION

It has become increasingly clear that the growth of central supermassive black holes (SMBHs) and their host spheroids are closely related since the mass of the SMBH correlates well with the properties of the hot stellar component of the host galaxy, e.g. the galactic velocity dispersion ( $M_{\text{BH}}\text{-}\sigma_*$ ), the luminosity/mass of the spheroidal component of the host galaxy (e.g. Magorrian et al. 1998; Ferrarese & Merritt 2000; Tremaine et al. 2002; Häring & Rix 2004). Hydrodynamical simulations on gas-rich galaxy mergers, incorporating star formation, SMBH growth and feedback from both supernovae and SMBH, provide a plausible picture of how galaxy formation and the growth of SMBHs are related to each other (e.g. Hopkins et al. 2006). However, much of the gas physics in numerical simulations, in particular how the star formation and central active galactic nucleus (AGN) activities feed energy and momentum back into the gas, is uncertain. Such feedbacks may heat up the cold gas and drive a powerful galactic wind or outflow, which may limit or even terminate further star formation and black hole growth in galaxies.

Hao et al. (2005, hereafter H05) studied a sample of type I active galactic nuclei (AGNs) selected from local ultraluminous infrared galaxies (ULIRGs, the  $8 - 1000\mu\text{m}$  integrated infrared luminosities are larger than  $10^{12}L_{\odot}$ ) and referred these as IR QSOs. By comparing IR QSOs with optically selected PG QSOs and narrow-line Seyfert 1s (NLS1s) in the relation of the IR luminosities versus the optical luminosities, they find that IR QSOs show mid-IR and far-IR (especially far-IR, hereafter FIR) excess. The FIR luminosities for most IR QSOs are larger than half of their central AGN bolometric luminosities. In contrast, the median ratio of the FIR to central AGN bolometric luminosities for local classical QSOs is four times smaller than that for IR QSOs. Comparisons of the FIR spectral index of IR QSOs with those of PG QSOs indicate that the FIR excess of IR QSOs relative to the PG QSOs is suggestive of massive starbursts. These IR QSOs not only have massive starbursts occurring in their host galaxies, but their optical spectroscopic and X-ray properties also exhibit characteristics of young, growing QSOs with high accretion rates to their central black holes (Zheng et al. 2002; H05). Moreover, images of these IR QSOs show that most are undergoing clear tidal interactions or major mergers (Canalizo & Stockton 2001; see also Fig.

1). The optical spectra show obvious blueshifts in permitted emission lines in some IR QSOs, indicating outflows. More recent IRAM Plateau de Bure Interferometer (PdBI) and Herschel observations of Mrk 231, the closest IR QSO, reveal clear outflows with velocity larger than  $1000 \text{ km s}^{-1}$ , as inferred from broad wings of the CO line or OH P-Cygni profile (Feruglio et al. 2010; Fischer et al. 2010) and the coexistence of active SMBH accretion and strong starburst (van der Werf et al. 2010). The mid-IR spectra of IR QSOs from *Spitzer*/Infrared Spectrograph (IRS) also show that the typical slope of spectral energy distribution (SED) for IR QSOs is between those of classical PG QSOs and ULIRGs (Cao et al. 2008). All the properties of IR QSOs are consistent with their being at an important transition stage from mergers with massive starbursts (ULIRGs) to dust-enshrouded QSOs and later luminous QSOs, and eventually early-type galaxies (Sanders et al. 1988a; Sanders & Mirabel 1996; Tacconi et al. 2002). Studies of these objects may thus provide significant insights into the understanding of how the growths of spheroids and SMBHs are inter-connected and how the  $M_{\text{BH}}-M_{\star}$  relation evolves as a function of redshift.

The conclusion that the FIR excess in IR QSOs is primarily due to starbursts requires a large reservoir of cold molecular gas in IR QSO hosts. In fact, up to now only 6 local IR QSOs (I Zw I, Mrk 231, Mrk 1014, 3C 48, IRAS 1613+658 and PG 1700+518) have been observed (Solomon et al. 1997; Schinnerer, Eckart & Tacconi 1998; Krips et al. 2005; Evans et al. 2001, 2009). The molecular gas masses of these IR QSO hosts are few times  $10^9$  to  $10^{10} M_{\odot}$ , assuming the same conversion factor from the CO luminosity to  $H_2$  mass as that for ULIRGs, i.e.  $\alpha_{\text{CO}} = 0.8 M_{\odot} (\text{K km s}^{-1} \text{ pc}^2)^{-1}$  (Downes & Solomon 1998). In contrast, the molecular gas masses of CO detected classical QSO hosts are at most a few times  $10^9 M_{\odot}$  (Evans et al. 2001; Scoville et al. 2003). The larger molecular gas reservoirs in these IR QSO hosts mean that there are rich of fuel to sustain the star formation and may support the speculation by Hao et al. (H05) that the FIR excess in IR QSOs is mainly due to starbursts. However, CO observations for a larger sample of IR QSOs are needed to statistically confirm this scenario.

As we will show later, in the IR QSO phase the SMBH and spheroid are both growing rapidly. Two questions naturally arise: What is the timescale for the consumption of the molecular gas to sustain the massive starbursts? Can the local  $M_{\text{BH}}-M_{\star}$  relation be established/maintained in this phase? Such a spheroid and central SMBH co-evolution process is expected to be more important at high redshift according to the downsizing galaxy formation scenario (Cowie et al. 1996). While a few tens of high-redshift QSOs have been detected in CO (Solomon & Vanden Bout 2005; Coppin et al. 2008; Wang et al. 2010; Riechers 2011a; Polletta et al. 2011), surprisingly only half a dozen local IR QSOs have been observed before this work. Clearly a larger local IR QSO sample detected in CO is desirable for comparisons with high-redshift CO detected QSOs. For all the above reasons, we have initiated a

program to observe a larger sample of IR QSOs with the IRAM 30m telescope in order to systematically investigate the molecular gas properties of these objects.

This paper presents the results of our CO observations of 19 IR QSOs with the IRAM 30m. The paper is structured as follows. In Sections 2 and 3, we describe our sample and outline the observations and data reduction respectively. We present our main results and discussion in Section 4, and a summary in Section 5. Throughout this paper we adopt a cosmology with a matter density parameter  $\Omega_m = 0.3$ , a cosmological constant  $\Omega_\Lambda = 0.7$  and a Hubble constant of  $H_0 = 70 \text{ km s}^{-1} \text{ Mpc}^{-1}$ .

## 2. SAMPLE

All of our 19 newly CO observed IR QSOs are selected from the IR QSO sample of H05 and have redshift  $z < 0.2$  except for  $F13218 + 0552$  ( $z=0.205$ ),  $F18216 + 6419$  ( $z=0.297$ ) and  $F02054 + 0835$  ( $z=0.345$ ). This IR QSO sample (H05) was compiled from the ULIRGs in the QDOT redshift survey (Lawrence et al. 1999), the 1 Jy ULIRG survey (Kim et al. 1998), and the cross-correlation of the IRAS Point Source Catalog (PSC) with the *ROSAT* All-sky Survey Catalog. We also include six previously published CO detections of IR QSOs. In total, our sample consists of 25 IR QSOs. As the fraction of IR QSOs in ULIRGs is less than 10% and the PSC IRAS redshift survey (Saunders et al. 2000) galaxy sample includes about 1000 ULIRGs, so the total number of IR QSOs expected in the northern sky is  $\lesssim 100$ . Our IR QSO sample includes about a quarter of the total, and thus should be a representative IR QSO sample in the local universe (see Zheng et al. 2002 for more detailed descriptions). Fig. 1 shows true color images of 12 IR QSOs (out of 25) cross-identified from DR7 of the Sloan Digital Sky Survey (SDSS). Most of these show tidal features and may be in the final merging stage.

For comparisons, we also compiled several samples with CO detections, including local ULIRGs, low-redshift classical QSOs and high-redshift (sub)millimeter (mm) luminous QSOs. Notice that we correct all the published results to our adopted cosmology. In the following, we briefly summarize these samples.

- (1) A ULIRG sample taken from Solomon et al. (1997) consists of 36 objects in the redshift range of  $z = 0.03$  to 0.27. The CO observations were made with the IRAM 30m telescope. There are more ULIRGs with CO observations (e.g., Chung et al. 2009; Mirabel et al. 1990), but here we restrain ourselves to systems with IRAM 30m data.
- (2) A local classical QSO sample with CO detections is compiled from 11 PG QSOs (Evans et al. 2001; Scoville et al. 2003) and 16 HE QSOs (Bertram et al. 2007), after

excluding several IR QSOs. Evans et al. (2001) selected their sample by IR excess ( $L(8-1000\mu\text{m})/L(0.1-1.0\mu\text{m}) > 0.36$ ) in the redshift range of  $0.04 < z < 0.17$ , while Scoville et al. (2003) selected their PG QSO sample with criteria of  $z < 0.1$  and  $M_B < -23$  mag. The HE QSO sample is a nearby low-luminosity QSO sample with redshift  $z < 0.06$ , drawn from the Hamburg-ESO survey for bright UV-excess QSOs and observed also by the IRAM 30m telescope (Bertram et al. 2007).

- (3) The (sub)mm luminous high-redshift QSO sample of 29 objects is taken from Wang et al. (2010). They observed six (sub)mm luminous QSOs with  $z \sim 6$  by the IRAM PdBI; for each object, either the CO(6-5) or (5-4) line emission has been detected. They also included two QSOs at  $z \sim 6$  previously detected in CO and another 21 high-redshift CO detected QSOs in the range of  $1.4 \leq z \leq 5$  from the literature. Notice that this CO detected, high-redshift (sub)mm luminous QSO sample includes nearly all such objects up to 2010.

### 3. OBSERVATIONS, DATA REDUCTION and PARAMETER ESTIMATION

The CO observations were carried out with the IRAM 30m telescope on Pico Veleta near Granada, Spain. Although the first of such attempts was conducted remotely from the IRAM headquarter in Grenoble in July 2007, the weather was mostly bad then and essentially little useful data were obtained. The data used here were mainly collected during the summer and autumn of 2008. Both the 3mm and 1mm dual-polarization receivers were used together with the  $512 \times 1$  MHz and  $256 \times 4$  MHz filter banks to simultaneously obtain both CO (1–0) and CO (2–1) emission lines. The weather was mostly excellent during these observing runs, but some CO (2–1) lines were still not observed for a few targets since the line frequencies were redshifted out of the tuning range of 1mm receivers. All observations were done with a wobbler switching mode with a throw rate of 0.5 Hz and a wobbler throw of  $60''$  in azimuth. System temperatures were on average  $T_{\text{sys}} \approx 150$  K and 450 K at  $\sim 105$  GHz and  $\sim 210$  GHz, respectively. The total usable on-source integration time is  $\sim 50$  hours from the 2008 runs. Table 1 summarizes the details of CO observations for all 19 sources.

We reduced the data using the IRAM software CLASS/GILDAS. First, we discarded a few bad scans with strongly distorted baselines, fixed some bad channels before summing up all scans to look for the likely detected CO line emission windows. We then subtracted linear baselines in each of the remaining scans with the adopted velocity windows before summing up to obtain the final spectra that are further subtracted with linear baselines. In order to increase the signal-to-noise ratio, all the spectra were Hanning smoothed to velocity

widths of  $> 20 \text{ km s}^{-1}$ . The amplitudes of each spectrum were converted to main beam temperatures,  $T_{\text{mb}}$ , by multiplying  $T_{\text{A}}^*$  by the ratio between the forward efficiency and main beam efficiency  $F_{\text{eff}}/B_{\text{eff}}$ . The main beam efficiency  $B_{\text{eff}} = 0.75$  and the forward efficiency  $F_{\text{eff}} = 0.95$  were applied to  $T_{\text{A}}^*$  at  $\sim 105 \text{ GHz}$  and  $B_{\text{eff}} = 0.57$  and  $F_{\text{eff}} = 0.91$  to  $T_{\text{A}}^*$  at  $\sim 210 \text{ GHz}$ , respectively. For point sources, flux densities were obtained using the conversion factor  $S_{\nu}/T_{\text{mb}} = 4.95 \text{ Jy/K}$  for the IRAM 30m telescope.

The CO line luminosities  $L'_{\text{CO}}$  for IR QSOs were calculated following Solomon, Downes, & Radford (1992)

$$L'_{\text{CO}} = 23.5 \Omega_{\text{S}^* \text{B}} D_{\text{L}}^2 I_{\text{CO}} (1+z)^{-3} [\text{K km s}^{-1} \text{ pc}^2], \quad (1)$$

where  $I_{\text{CO}}$  is the velocity-integrated line intensity in units of  $\text{K km s}^{-1}$ ,  $D_{\text{L}}$  is the luminosity distance measured in Mpc, and  $\Omega_{\text{S}^* \text{B}}$  is the solid angle of the source convolved with the telescope beam in square arc-seconds, i.e.  $\Omega_{\text{S}^* \text{B}} = \frac{\pi}{4 \ln 2} (\theta_{\text{S}}^2 + \theta_{\text{B}}^2)$ , where  $\theta_{\text{B}} = 24''$  at  $105 \text{ GHz}$ .

The CO luminosities for PG and HE QSOs were estimated using the same method and were provided in the respective papers described in §2. We simply adapted them to our adopted cosmology. For the high-redshift QSO sample collected by Wang et al. (2010), a different approach was applied since most of these objects were detected at high orders ( $J > 5$ ) of CO transitions. Wang et al. (2010) calculated the  $L'_{\text{CO}(1-0)}$  values for all high- $z$  sample QSOs under the non-thermalized excitation assumption and adopted the line ratios of CO (6–5)/CO (1–0) and CO (5–4)/CO (1–0) as 0.78 and 0.88, respectively. Since only the CO ground state transition CO (1–0) traces molecular gas at low excitation and provides a direct estimate of the total cold molecular gas mass (Riechers et al. 2007, 2011b; Gao & Solomon 2004a), we will use either the observed and/or converted CO (1–0) properties for all QSOs at different redshifts in this work.

Apart from CO line luminosities, FIR luminosities are needed as well in this work. The FIR luminosities ( $L_{\text{FIR}}$ , the luminosity in the range of  $42.5\text{--}122.5 \mu\text{m}$ ) were calculated based on the flux densities at  $60 \mu\text{m}$  and  $100 \mu\text{m}$  from the IRAS Faint Source Catalog for local IR QSOs, ULIRGs and PG+HE QSOs, following Helou et al. (1988). For high-redshift (sub)mm loud QSOs, their FIR luminosities were provided by Wang et al. (2010; private communication); they derived  $L_{\text{FIR}}$  based on (sub)mm continuum measurements under the assumption that the rest-frame FIR SED can be described by a grey-body spectrum with a dust temperature of  $47 \text{ K}$  and emissivity index of  $1.6$  (Beelen et al. 2006) except for J1148+5251 and J0927+2001. For these two objects, Wang et al. (2010) used a fitted temperature of  $56 \text{ K}$  and  $46 \text{ K}$  respectively.

We also need the AGN-associated bolometric luminosities  $L_{\text{AGN}}$  for our QSO samples (hereafter we use  $L_{\text{AGN}}$  to denote the bolometric luminosities from AGN for all QSOs).

For local PG QSOs and IR QSOs, they were estimated from the extinction corrected continuum emission at  $5100\text{\AA}$  and adopting a bolometric correction factor of 9, i.e.,  $L_{\text{AGN}} \approx 9\lambda L_{\lambda}(5100)\text{\AA}$  (H05). For HE QSOs, the central AGN bolometric luminosities  $L_{\text{AGN}}$  were derived from their  $B_J$  magnitudes with a bolometric correction factor of 9.74 (Vestergaard et al. 2004). For the 11 high-redshift QSOs in Hao et al. (2008),  $L_{\text{AGN}}$  were taken from that paper directly, calculated in the same way as for HE QSOs. For the eight  $z \sim 6$  QSOs, the absolute AB magnitudes at rest frame  $1450\text{\AA}$  derived by Wang et al. (2010) were converted into the B band magnitudes according to Schmidt et al. (1995; see also Fan et al. 2001), and then a bolometric correction factor of 9.74 was employed to convert the B-band magnitudes into  $L_{\text{AGN}}$ . For the ten high-redshift QSOs neither in Hao et al. (2008) nor in Wang et al. (2010), we computed their  $L_{\text{AGN}}$  in the same way as Hao et al. (2008).

## 4. RESULTS AND DISCUSSIONS

### 4.1. CO Emissions from IR QSO hosts

17 out of the 19 new IR QSO hosts have been detected in CO (1–0), while nine of them have also been observed and all detected in CO (2–1). All the detections except for F12265+0219 and F12134+5459 (which were marginally detected at  $3\sigma$ ) have signal-to-noise ratio (S/N) greater than  $5\sigma$ . Fig. 2 presents the CO (1–0) and CO (2–1) spectra for all IR QSOs. Those targets without CO (2–1) lines are simply redshifted out of tunable range of the 1mm receivers and thus cannot be observed. We also calculated the  $3\sigma$  upper limits (about  $10^{10} \text{ K km s}^{-1} \text{ pc}^2$ ) for the two non-detections by assuming a line width (Full Width at Zero Intensity, hereafter FWZI) of  $600 \text{ km s}^{-1}$ . The reasons for non-detections (for IRAS F18216+6419 and IRAS F02054+0835) may be that the integration time is insufficient because these two objects have the highest redshifts in our sample.

The CO (1–0) and CO (2–1) line widths (FWZI), integrated line luminosity, FIR luminosity and  $L_{\text{FIR}}/L'_{\text{CO}(1-0)}$  for all our sample objects, including 6 IR QSOs from the literature, are listed in Table 2. From this table, we can see that the CO luminosities ( $L'_{\text{CO}}$ ) for the 23 CO detected IR QSO hosts (17 of which are from our sample) are several times  $10^9$  to a few times  $10^{10} \text{ K km s}^{-1} \text{ pc}^2$ , comparable to those for ULIRGs with the largest molecular gas reservoirs in the local universe. The upper limits of the two non-detections are also consistent with this mass range.

The CO (2–1)/CO (1–0) line luminosity ratio ( $r_{21}$ ) ranges from 0.4 to 1.2 with mean value of  $\sim 0.8$  in nine CO (2–1) detected IR QSOs. Four IR QSOs out of nine are found to have  $r_{21} \geq 1$  with uncertainty of  $\sim 15\%$ , suggesting that the molecular gas is essentially

thermalized and has a point-like distribution compared to the  $12''$  CO(2–1) beam (corresponding to 24 kpc for the median redshift of CO (2–1) detected IR QSOs,  $z \sim 0.11$ ). Three IR QSOs have  $r_{21} \sim 0.7$  with uncertainty of  $\sim 12\%$ , a typical average value for ULIRGs (Radford, Downes & Solomon 1991), which implies they, similar to ULIRGs, have modest sub-thermal molecular gas properties. Furthermore, if they are indeed sub-thermally excited with such line ratios, then these sources again have point-like molecular gas distribution compared to the  $12''$  beam. Only 2 IR QSOs have really low  $r_{21}$  ratios ( $\sim 0.5$ ) with uncertainty of  $\sim 10\%$ , which may be due to their sub-thermalized molecular gas properties and/or their extended spatial structure (Garay, Mardones & Mirabel 1993) of quite a few arc-seconds. From our limited CO (2–1) data, we infer that the molecular gas distributions in most (7 out of 9) IR QSOs are probably concentrated in compact nuclear regions. However, further high spatial resolution observations, e.g., Aravena et al. (2011), are needed to reveal the spatial distribution and kinematics of the molecular gas in IR QSOs.

#### 4.2. Comparison with Local ULIRGs

Fig. 3 compares the CO properties of IR QSO hosts (upper panels) with those of ULIRGs (lower panels). Specifically, the histograms of the CO luminosity ( $L'_{\text{CO}(1-0)}$ ) (left panels), the FIR to CO luminosity ratio  $L_{\text{FIR}}/L'_{\text{CO}}$  (commonly used as an indicator of the star formation efficiency [SFE], middle panels) and CO (1–0) line width (FWHM, right panels) are compared. Median and mean values are labelled in the upper left corner of the panels.

From Fig. 3 we can see that the median value of  $L'_{\text{CO}(1-0)}$  for IR QSO hosts is similar to that of ULIRGs. Hence, the molecular gas in IR QSO hosts is as abundant as in ULIRGs which can easily provide the fuel needed for their ongoing starbursts. In addition, the median values of  $L_{\text{FIR}}/L'_{\text{CO}}$  (SFE) and CO line width for IR QSO hosts are also similar to those of ULIRGs at the  $3\sigma$  level. IR QSO hosts appear to have similar SFRs, velocity spread in CO, and SFEs as ULIRGs, likely though ULIRGs have evolved into the QSO episode manifested as IR QSOs.

It is widely accepted that the FIR emission of ULIRGs is mainly from star formation (e.g. Yun et al. 2001; Gao & Solomon 2004b) and most molecular gas in ULIRGs is distributed in centrally rotating nuclear disks or rings as revealed by CO images (Downes & Solomon 1998). The similarities of IR QSO hosts and ULIRGs in their CO properties suggest that their FIR luminosities are both dominated by dust heated by starbursts and even their cold molecular gas may have similar spatial distributions. In fact, the highest resolution CO interferometer observations for two IR QSOs, Mrk 231 and I Zw I show nuclear disks and rings. For Mrk 231, there is an inner disk of diameter  $1.2''$  (radius  $\sim 0.5$  kpc) and an outer



disk with diameter of  $3''$  (radius  $\sim 1.25$  kpc, Downes & Solomon 1998). For I Zw I, there is a ring-like structure of radius 1.2 kpc (Staguhn et al. 2004). Our available line ratios of  $r_{21}$  are also consistent with the CO emission in IR QSOs being mostly concentrated in nuclear regions. If most IR QSO hosts indeed have similar CO properties to those of ULIRGs, it follows that the CO-to- $H_2$  conversion factor from  $L'_{CO}$  to cold molecular gas mass for IR QSOs should be the same for ULIRGs, i.e.  $\alpha_{CO} = 0.8M_{\odot} (\text{K km s}^{-1} \text{ pc}^2)^{-1}$ . Therefore, the cold molecular gas properties, such as cold molecular gas mass, SFE, and possibly the spatial distribution in IR QSOs, are indistinguishable from those of ULIRGs.

Taking into account the properties of IR QSOs in different wavebands, such as the optical morphology, extreme Fe II emissions in their optical spectra (Zheng et al. 2002), FIR excess emissions compared with classical QSOs (H05) and similar  $6.2\mu\text{m}$  PAH and [NeII]  $12.81\mu\text{m}$  emission strengths in IR QSO and ULIRGs (Cao et al. 2008), there is little doubt that there are ongoing massive starbursts in IR QSO hosts, as in ULIRGs. The timescale of starbursts in IR QSOs is about a few times  $10^7$  yr, as inferred from  $M_{\text{gas}}/\text{SFR}$  by assuming that the FIR emission is predominately from star formation (see Table 3).

### 4.3. Comparison with Local and High-redshift CO-detected QSOs

Fig. 4 presents the  $L_{\text{FIR}}$  versus  $L'_{CO(1-0)}$  relation for almost all local and high-redshift QSOs with CO detections up to 2010. Throughout this paper, the red filled squares represent the local IR QSOs, black open pentagrams denote the local PG and HE QSOs and blue crosses represent the high-redshift QSOs. It is clear from Fig. 4 that there is a tight correlation between  $L_{\text{FIR}}$  and  $L'_{CO(1-0)}$ , spanning four and three orders of magnitude in  $L_{\text{FIR}}$  and  $L'_{CO(1-0)}$ , respectively. The Spearman Rank-order (S-R) correlation analysis gives a coefficient of 0.94 with significance of  $> 99.99\%$ . Such a strong correlation between  $L_{\text{FIR}}$  and  $L'_{CO(1-0)}$  for all CO detected QSOs seems to suggest that the bulk of FIR emissions from all QSOs are from the same origin (star formation), since similar correlations are well established for star-forming galaxies at both low and high redshifts (e.g. Solomon & Vanden Bout 2005; Riechers 2011a). The best-fit power-law slope between  $L_{\text{FIR}}$  and  $L'_{CO(1-0)}$  is approximately 1.4 regardless of the sample QSOs included. This is different from star-forming galaxies where the best-fit slope varies from 1 to 1.7 depending on how many ULIRGs are included (Gao & Solomon 2004b).

The nonlinear correlation between  $L_{\text{FIR}}$  and  $L'_{CO(1-0)}$  for local star-forming galaxies, luminous starbursts, ULIRGs and high-redshift CO detected objects has been widely discussed and is likely due to different dense molecular gas fractions in different classes of objects (Gao & Solomon 2004b; Daddi et al. 2010). Our super-linear power-law slope (1.4) is consistent

with their conclusion. Furthermore, Fig. 5 shows the luminosity ratio  $L_{\text{FIR}}/L'_{\text{CO}(1-0)}$  as functions of FIR luminosities  $L_{\text{FIR}}$  (left panel) and CO (1-0) luminosities  $L'_{\text{CO}(1-0)}$  (right panel). It is clear from Fig. 5 that there are tight correlations between  $L_{\text{FIR}}/L'_{\text{CO}(1-0)}$  and  $L_{\text{FIR}}$ , as well as between  $L_{\text{FIR}}/L'_{\text{CO}(1-0)}$  and  $L'_{\text{CO}(1-0)}$ . Notice that unlike Fig. 4, the vertical axis does not depend on the distance. The S-R correlation analysis gives a coefficient of 0.83 and 0.59, respectively, and both with significance level larger than 99.99%. Gao & Solomon (2004b) showed that  $L_{\text{FIR}}/L'_{\text{CO}(1-0)}$  is proportional to the dense molecular gas fraction as measured by  $L_{\text{HCN}}/L'_{\text{CO}(1-0)}$ , where HCN is the most abundant high dipole-moment molecules. The correlations shown in Fig. 5 indicate that the dense molecular gas fraction might increase with increasing FIR luminosities and CO (1-0) luminosities ( $L'_{\text{CO}(1-0)}$ ) for all CO detected QSOs.

We also collected polycyclic aromatic hydrocarbon (PAH)  $6.2\mu\text{m}$  emission data from the IRS on *Spitzer* (Houck et al. 2004) for our IR QSO sample and other CO detected QSOs (Lutz et al. 2008; Cao et al. 2008). Fig. 6 shows the correlation between  $L_{6.2\mu\text{m}}$  and  $L'_{\text{CO}(1-0)}$  for all sample QSOs with  $6.2\mu\text{m}$  measurements including some upper limits. Since the  $6.2\mu\text{m}$  PAH emission is believed to originate from star formation, the correlation shown in Fig. 6 further confirms the star formation origin of the FIR emission for all QSOs. Netzer et al. (2007) reached the same conclusion based on their analysis of the SED of QSOs and ULIRGs observed by *Spitzer*/IRS. Our results further strengthen the conclusion: even in the QSO episode, the large amount of cold molecular gas reservoir still serves as the fuel to sustain star formation seen in the FIR emission.

We now return to discuss Fig. 4. A closer examination of this figure reveals that the correlation between  $L_{\text{FIR}}$  and  $L'_{\text{CO}(1-0)}$  for QSOs shown in Fig. 4 is tighter than that for all star-forming galaxies, such as local spiral galaxies, ULIRGs and submm galaxies (SMGs, e.g., Fig. 8 in Bertram et al. 2007). It appears to suggest that the cold molecular gas properties (distribution) in QSO hosts is not as complicated as those in starbursts, ULIRGs and/or SMGs.

This point is supported by different spatial distributions of molecular gas in these objects. High resolution CO observations for local IR QSOs (e.g., Mrk 231 and I Zw I, as described in §4.2) and high-redshift (sub)mm detected QSOs (e.g. APM 08279+5255, Cloverleaf QSO, J1148+5251) show that the molecular gas in these QSO hosts are concentrated in central disks/rings with radius on the order of 1 kpc (Solomon et al. 2003; Staguhn et al. 2004; Riechers et al. 2009; Walter et al. 2009). Bradford et al. (2009) reached the same conclusion from analyses of many molecular line species from the single-dish observations of the Cloverleaf. In contrast, a significant fraction of ULIRGs and SMGs are interacting or merging galaxy pairs with wide separations. In this case, a lot of the cold molecular

gas has not yet settled into nuclear rotating disks/rings, instead, the gas is still very extended spatially and likely has different physical parameters from the molecular gas in the disks (Dinh-V-Trung et al. 2001; Greve et al. 2005; Tacconi et al. 2008; Riechers et al. 2011c), which may have contributed to the larger scatters in the correlation between  $L_{\text{FIR}}$  and  $L'_{\text{CO}(1-0)}$ .

Further evidence for different sizes is provided by recent high resolution observations of SMGs and lensed high- $z$  QSOs (Casey et al. 2011; Riechers et al. 2011c, 2011d), which reveal extended cold molecular gas components in SMGs, but not in lensed QSOs. The tighter correlation between  $L_{\text{FIR}}$  and  $L'_{\text{CO}(1-0)}$  for QSOs, as shown in Fig. 4, is consistent with different spatial distributions of molecular gas between QSOs and ULIRGs/SMGs.

From Fig. 4, one can also see that while most CO detected QSOs at high-redshift are more luminous, nevertheless the local and high-redshift CO detected QSOs form a continuous sequence. In particular, four high-redshift CO detected QSOs have CO luminosities comparable to local IR QSOs. The comparable CO and FIR luminosities imply similarities between these high-redshift QSOs and local IR QSOs in both cold molecular gas contents and SFRs. Due to sensitivity limits of current facilities, observations of FIR and CO faint QSOs are usually for gravitationally lensed systems: three of these four relatively faint high-redshift QSOs are lensed (SMM 04135, IRAS F10214 and Cloverleaf). Most recently, Riechers (2011a) reported CO detections for four additional lensed high-redshift QSOs with relatively low  $L_{\text{FIR}}$  and  $L'_{\text{CO}(1-0)}$  by the Combined Array for Research in Millimeter-wave Astronomy (CARMA). Again, the intrinsic FIR and CO luminosities of these high-redshift QSOs are comparable to our IR QSOs. The similarities can be further verified when more observations of fainter (unlensed) high-redshift QSOs become available with the Atacama Large (sub-) Millimeter Array (ALMA) in the near future.

#### 4.4. the Evolution from Massive Starbursts to Luminous QSOs

It is widely accepted that the growth of central SMBHs and their host spheroids are closely related due to the local SMBH-spheroid mass relation (Magorrrain et al. 1998; Ferrarese & Merritt 2000; Tremaine et al. 2002). This close connection is also mirrored in similar shapes in the cosmic history of black hole growth and star formation (e.g. Merloni et al. 2004). It is suggestive of a possible coeval evolution of central SMBHs and their spheroids. However, it is still unclear how or even whether spheroids of galaxies co-evolve with their central SMBHs at all stages. In the following, we examine more closely the relation between the accretion rate of central SMBHs and SFRs in the host galaxies for all CO detected QSOs.

Fig. 7 shows the AGN-associated bolometric luminosities ( $L_{\text{AGN}}$ ) vs.  $L'_{\text{CO}(1-0)}$  for all CO detected QSOs. Note that the AGN-associated bolometric luminosities used in this paper are the integrated luminosities over the SEDs for the AGN components, as described in §3. From Fig. 7, we can see clearly that as  $L'_{\text{CO}(1-0)}$  increases,  $L_{\text{AGN}}$  also increases. The Spearman Rank-order correlation analysis gives a coefficient of 0.83 with significance  $> 99.99\%$ . A least-square bisector fit for low-redshift CO detected PG and HE QSOs in Fig. 7 yields a best-fit slope of  $1.4 \pm 0.2$ . The correlation between  $L_{\text{AGN}}$  and  $L'_{\text{CO}(1-0)}$  is suggestive of some link between the cold molecular gas on  $\sim \text{kpc}$  scale disks/rings and the central SMBH accretion process on much smaller scales - it is likely that both nuclear star formation and SMBH accretion rely on the same molecular gas reservoir (Bonfield et al. 2011; Diamond-Stanic & Rieke 2011).

It is interesting that all IR QSOs and the few relatively faint high-redshift QSOs with  $L_{\text{AGN}}$  less than  $\sim 10^{13}L_{\odot}$  are located on or below the best-fit line, while most high-redshift QSOs with  $L_{\text{AGN}}$  larger than  $\sim 10^{13}L_{\odot}$  are located above. Such a systematic difference in the locations on Fig. 7 for IR QSOs and most high-redshift optically bright QSOs could reflect some intrinsic difference in the properties between these two populations, although some selection effects may have also played a role.

The  $L_{\text{AGN}}/L'_{\text{CO}}$  ratio relates to the accretion efficiency to central SMBH, as indicated by  $\dot{M}_{\text{acc}}/M_{\text{gas}}$ . Fig. 8 compares the histograms of  $L_{\text{AGN}}/L'_{\text{CO}}$  for CO detected local IR QSOs, PG+HE QSOs and high-redshift QSOs (top, middle and bottom panels respectively). A comparison of the top and middle panels shows that the median value of  $L_{\text{AGN}}/L'_{\text{CO}}$  for local PG+HE QSOs is larger than that for IR QSOs. Since a large fraction of optically bright PG QSOs are CO non-detected (or not observed), the real median value of  $L_{\text{AGN}}/L'_{\text{CO}}$  for classical QSOs should be even higher than the plotted one. The difference of the  $L_{\text{AGN}}/L'_{\text{CO}}$  ratios between IR QSOs and the brightest high-redshift QSOs is even more dramatic, about one order of magnitude.

In order to understand why the  $L_{\text{AGN}}/L'_{\text{CO}}$  ratios for local PG+HE QSOs and high-redshift QSOs are much higher than those of IR QSOs, we plot the histograms of  $L_{\text{FIR}}/L_{\text{AGN}}$  in Fig. 9 for these three classes of objects. For local classical QSOs and the brightest high-redshift QSOs, the FIR luminosities are  $\gtrsim 10\%$  of their central AGN bolometric luminosities, so the main energy output for these QSOs is dominated by central AGNs, rather than starbursts. In contrast, the median  $L_{\text{FIR}}/L_{\text{AGN}}$  value for IR QSOs is  $\sim 0.6$ , indicating that the FIR luminosities of most IR QSOs are comparable to their central AGN bolometric luminosities.

The ratio of central SMBH accretion rate to the SFR in their host galaxies ( $\dot{M}_{\text{acc}}/\text{SFR}$ )

can be estimated by  $L_{\text{AGN}}/L_{\text{FIR}}$  based on the following equation:

$$\dot{M}_{\text{acc}}/\text{SFR} = 2.1L_{\text{AGN}}/L_{\text{FIR}} \times 10^{-3}, \quad (2)$$

assuming an accretion efficiency  $\eta = 0.1$  (see Hao et al. 2008). Although the uncertainties are large due to a number of assumptions on determining these key parameters, we can nevertheless roughly estimate whether SMBHs and their host galaxies co-evolve based on the  $L_{\text{FIR}}/L_{\text{AGN}}$  ratio.

As can be seen from Fig. 9, the median values of  $L_{\text{FIR}}/L_{\text{AGN}}$  are about 0.58, 0.16 and 0.13 for IR QSOs, local PG+HE QSOs and high-redshift QSOs, respectively. The corresponding median values of  $\dot{M}_{\text{acc}}/\text{SFR}$  are  $3.6 \times 10^{-3}$  for IR QSOs, and  $1-2 \times 10^{-2}$  for local PG+HE QSOs and high-redshift brightest QSOs (see also Coppin 2009). So the  $\dot{M}_{\text{acc}}/\text{SFR}$  value for IR QSOs is comparable to that of local  $M_{\text{BH}}/M_{\text{sph}}$  value,  $\sim 1.4 \times 10^{-3}$  (Häring & Rix 2004), implying their central SMBHs and host spheroids grow in line with the local relation. In contrast, the  $\dot{M}_{\text{acc}}/\text{SFR}$  values for local classical QSOs and high-redshift bright QSOs are almost an order of magnitude larger than the local  $M_{\text{BH}}/M_{\text{sph}}$  value. For these objects, the central SMBH masses increase much faster than their host spheroids compared to the local scaling. It is interesting to note that the four relatively faint high-redshift CO detected QSOs (SMM 04135, F 10214, Cloverleaf and RXJ 124913) have high  $L_{\text{FIR}}/L_{\text{AGN}}$  values that are close to or even larger than those of local IR QSOs, thus the growth of their black hole may be slower than that of high-luminosity QSOs.

According to the scenario first pointed out by Sanders et al. (1988a, b), IR QSOs will eventually evolve toward classical QSOs. The different efficiencies of gas accretion to central SMBH ( $\dot{M}_{\text{acc}}/M_{\text{gas}}$ ) between the IR QSOs and local classical QSOs and the high-redshift brightest QSOs then fit well into a picture where the QSO luminosity reaches the maximum when the star formation at the central  $\sim \text{kpc}$  decreases to a few tenths of its peak value and no longer dominates the energy output (as indicated by the  $L_{\text{FIR}}/L_{\text{AGN}}$  value). Such an evolutionary path has also been discussed for AGNs in SMGs by Alexander (2009) and is broadly consistent with the simulation results of Hopkins (2011).

We can also obtain more quantitative estimates of the star formation timescales and black hole masses. Table 3 lists the median values of SFR,  $\dot{M}_{\text{acc}}$ ,  $M_{\text{BH}}$ , cold molecular gas mass  $M_{\text{gas}}$  and dynamical mass  $M_{\text{dyn}}$  for IR QSOs, PG+HE QSOs and high-redshift QSOs. The SFRs and accretion rates are estimated from  $L_{\text{FIR}}$  and  $L_{\text{AGN}}$  following Hao et al. (2008), the SMBH masses are taken from the literature, while gas masses are estimated from  $L'_{\text{CO}(1-0)}$  and dynamical masses are estimated from the stellar CO absorption line widths in the H-band (Dasyra et al. 2006) for local QSOs and CO line widths for high-redshift QSOs. Such dynamical masses should be treated as upper limits of the stellar mass of QSO's host galaxies (e.g. Coppin et al. 2008).

First, we notice that the timescale for the gas consumption is on the scale of a few times  $10^7$  yr for all types of objects. Second, the  $M_{\text{BH}}/M_{\text{dyn}}$  for PG QSOs is  $10^{-3}$ , similar to the value for local galaxies, again indicating that PG QSOs follow the local scaling relation (Dasyra et al. 2006). However, the  $M_{\text{BH}}/M_{\text{dyn}}$  values are quite different,  $4.5 \times 10^{-4}$  and  $10^{-2}$  for IR QSOs and the brightest high-redshift CO detected QSOs, respectively. The SMBHs in IR QSOs appear to be below the local  $M_{\text{BH}}$  and  $M_{\text{sph}}$  relation, whereas the SMBHs in the brightest high-redshift CO detected QSOs are much larger than that predicted by the local relation. It suggests that while star formation and AGN activities are intimately connected, they are not necessarily synchronized, as also suggested by numerical simulations (Hopkins 2011). In particular, IR QSOs appear to be in a transition stage with a timescale of a few times  $10^7$  yr; the rapid accretion (with  $\dot{M}_{\text{acc}} \sim 1 M_{\odot} \text{yr}^{-1}$ ) can grow the mass of a black hole up to a few times  $10^8 M_{\odot}$  after this phase. Henceforth it may follow the  $M_{\text{BH}}$  vs.  $M_{\text{sph}}$  relation seen in local galaxies.

## 5. SUMMARY

In this paper we report the detections of cold molecular gas in 17 out of 19 infrared ultraluminous QSO (IR QSOs) hosts observed using the IRAM 30m telescope. Including six additional IR QSOs with CO detections from the literature, our IR QSO sample consists of 25 objects with 23 detections. The gas reservoir in these objects is found to be several times  $10^9 M_{\odot}$  to a few times  $10^{10} M_{\odot}$ . Comparisons with local ULIRGs indicate that the cold molecular gas properties, such as the cold molecular gas mass content, star formation efficiency, and the CO (1-0) line widths of IR QSO hosts are similar to those of ULIRGs. These results suggest that sufficient amount of cold molecular gas exists to sustain massive starbursts even in the ultraluminous IR QSOs phase.

We also compared the IR QSO properties with several other QSO samples with molecular gas detections at both low and high redshifts. Our main findings are summarized as follows.

1. There exists a tight correlation between  $L_{\text{FIR}}$  and  $L'_{\text{CO}(1-0)}$  for all QSOs, spanning four and three orders of magnitude in  $L_{\text{FIR}}$  and  $L'_{\text{CO}(1-0)}$ , respectively. The  $6.2\mu\text{m}$  PAH luminosity ( $L_{6.2\mu\text{m}}$ ) and  $L'_{\text{CO}(1-0)}$  are also closely correlated for all sample QSOs. It seems to confirm the results based on *Spitzer*/IRS observations that the FIR emissions of all QSOs are mainly from star formation process rather than AGN. From this correlation as well as our limited CO line ratio measurements for IR QSOs and available CO images of QSOs, we speculate that the geometry of cold molecular gas for most QSOs at both high-redshift and low-redshift could be in a disk/ring on  $\sim$  kpc scale,

similar to those seen in some local ULIRGs.

2. The AGN-associated bolometric luminosities of all QSOs increase as  $L'_{\text{CO}}$  increases, implying a possible link between the cold molecular gas on  $\sim$  kpc scale (disk/ring) and the central black hole accretion process. Thus it is likely that both star formation and central black hole accretion draw from the same cold molecular gas reservoir.
3. The  $\dot{M}_{\text{acc}}/\text{SFR}$  values for IR QSOs and a few high-redshift, relatively faint QSOs are comparable to the local  $M_{\text{BH}}/M_{\text{sph}}$  value. These QSOs might be in the transition stage from gas-rich galaxy mergers to QSOs then to elliptical galaxies, exhibiting both high SFR and high accretion rates. However, the local  $M_{\text{BH}}/M_{\text{sph}}$  relation could not be established in this short transition phase. If the black hole continues to grow vigorously after this transition period, then the  $M_{\text{BH}}/M_{\text{sph}}$  relation may be established afterwards. On the other hand, for both local and very bright high-redshift QSOs, the black hole appears to grow much faster than the spheroids. It remains to be seen how the  $M_{\text{BH}}$  vs.  $M_{\text{sph}}$  evolves as a function of cosmic time.

This work is based on observations carried out with the IRAM 30m telescope. IRAM is supported by INSU/CNRS (France), MPG (Germany) and IGN (Spain). We thank Drs. J. S. Huang and J. M. Wang for advice and helpful discussions. We also thank Drs. Thomas Bertram and Lutz Wisotzki for kindly providing us with the unpublished  $B_J$  magnitudes for HE QSOs, and Dr. Ran Wang for providing us data for high-redshift QSOs. This project is supported by the NSF of China 10833006, 10973011, 11003015, 11173059 and 973 project (2007CB815405) and Chinese Academy of Sciences (SM).

## REFERENCES

- Alexander, D. M. 2009, ASPC, 408, 423
- Aravena, M., Wagg, J., Papadopoulos, P. P., & Feain, I. J. 2011, ApJ, 737, 64
- Beelen, A., Cox, P., Benford, D. J., et al. 2006, ApJ, 642, 694
- Bertram, T., Eckart, A., Fischer, S., et al. 2007, A & A, 470, 571
- Bonfield, D. G., Jarvis, M. J., Hardcastle, M. J., et al. 2011, MNRAS, 416, 13
- Bradford, C. M., Aguirre, J. E., Aikin, R., et al. 2009, ApJ, 705, 112
- Canalizo, G., & Stockton, A. 2001, ApJ, 555, 719

- Cao, C., Xia, X. Y., Wu, H., et al. 2008, MNRAS, 390, 336
- Casey, C. M., Chapman, S. C., Neri, R., et al. 2011, MNRAS, 415, 2723
- Chung, A., Narayanan, G., Yun, M. S., Heyer, M., & Erickson, N. R. 2009, AJ, 138, 858
- Coppin, K. E. K. 2009, ASPC, 408, 399
- Coppin, K. E. K., Swinbank, A. M., Neri, R., et al. 2008, MNRAS, 389, 45
- Cowie, L. L., Songaila, A., Hu, E. M., & Cohen, J. G. 1996, AJ, 112, 839
- Daddi, E., Elbaz, D., Walter, F., et al. 2010, ApJ, 714, 118
- Dasyra, K. M., Tacconi, L. J., Davies, R. I., et al. 2006, ApJ, 651, 835
- Dasyra, K. M., Tacconi, L. J., Davies, R. I., et al. 2007, ApJ, 657, 102
- De Rosa, G., Decarli, R., Walter, F., et al. 2011, ApJ, 739, 56
- Diamond-Stanic, A. M., & Rieke, G. H. 2011, ApJ, Submitted (arXiv:1106.3565)
- Dinh-V-Trung, Lo, K. Y., Kim, D.-C., Gao, Y., & Gruendl, R. A. 2001, ApJ, 556, 141
- Downes, D., & Solomon, P. M. 1998, ApJ, 507, 615
- Evans, A. S., Frayer, D. T., Surace, J. A., & Sanders, D. B. 2001, AJ, 121, 1893
- Evans, A. S., Hines, D. C., Barthel, P., et al. 2009, AJ, 138, 262
- Evans, A. S., Solomon, P. M., Tacconi, L. J., Vavilkin, T., & Downes, D. 2006, AJ, 132, 2398
- Fan, X. H., Strauss, Michael A., Richards, Gordon T., et al. 2001, AJ, 121, 31
- Ferrarese, L., & Merritt, D. 2000, ApJ, 539, L9
- Feruglio, C., Maiolino, R., Piconcelli, E., et al. 2010, A & A, 518, L155
- Fischer, J., Sturm, E., González-Alfonso, E., et al. 2010, A & A, 518, L41
- Gao, Y., & Solomon, P. M. 2004a, ApJS, 152, 63
- Gao, Y., & Solomon, P. M. 2004b, ApJ, 606, 271
- Greve, T. R., Bertoldi, F., Smail, Ian, et al. 2005, MNRAS, 359, 1165



- Hao, C. N., Xia, X. Y., Mao, S., Deng, Z. G. & Wu, H. 2008, ChJAA, 8, 12
- Hao, C. N., Xia, X. Y., Mao, S., Wu, H., & Deng, Z. G. 2005, ApJ, 625, 78 (H05)
- Häring, N., & Rix, H.-W., 2004, ApJ, 604, L89
- Heckman, T. M., Chambers, K. C., & Postman, M. 1992, ApJ, 391, 39
- Helou, G., Khan, I. R., Malek, L., & Boehmer, L. 1988, ApJS, 68, 151
- Hopkins, P. F., Hernquist, L., Cox, T. J., et al. 2006, ApJS, 163
- Hopkins, P. F. 2011, MNRASLetters in press (arXiv1101.4230)
- Houck, J. R., Roellig, T. L., van Cleve, J., et al. 2004, ApJS, 154, 18
- Kim, D.-C., Veilleux, S., & Sanders, D. B. 1998, ApJ, 508, 627
- Krips, M., Eckart, A., Neri, R., et al. 2005, A&A, 439, 7
- Lawrence, A., Rowan-Robinson, M., Ellis, R. S., et al. 1999, MNRAS, 308, 897
- Lupton, R., Blanton, M. R., Fekete, G., et al. 2004, PASP, 116, 133
- Lutz, D., Sturm, E., Tacconi, L. J., et al. 2008, ApJ, 684, L853
- Magorrian, J., Tremaine, S., Richstone, D., et al. 1998, AJ, 115, 2285
- Matthews, L. D. & Gao, Y. 2001, ApJ, 549, L191
- Merloni, A., Rudnick, G., Di Matteo, T. 2004, MNRAS, 354, L37
- Mirabel, I. F., Booth, R.S., Garay, G., Johansson, L. E. B., & Sanders, D. B. 1990, A&A, 236, 327
- Netzer, H., Lutz, D., Schweitzer, M., et al. 2007, ApJ, 666, 806
- Polletta, M., Nesvadba, N. P. H., Neri, R., et al. 2011, A&A, 533, 20
- Riechers, D. A. 2011a, ApJ, 730, 108
- Riechers, D. A., Carilli, C. L., Maddalena, R. J., et al. 2011c, ApJ, 739, L32
- Riechers, D. A., Hodge, J., Walter, F., Carilli, C. L., & Bertoldi, F. 2011b, ApJ, 739, L31
- Riechers, D. A., Walter, F., Carilli, C. L., et al. 2007, IAUS, 235, 423

- Riechers, D. A., Walter, F., Carilli, C. L., & Lewis, G. F. 2009, *ApJ*, 690, 463
- Riechers, D. A., Walter, F., Carilli, C. L., et al. 2011a, *ApJ*, 726, 50
- Sanders, D. B., Soifer, B. T., Elias, J. H., et al. 1988, *ApJ*, 325, 74
- Sanders, D. B., Soifer, B. T., Elias, J. H., Neugebauer, G., Matthews, K. 1988, *ApJ*, 328, L35
- Sanders, D. B., & Mirabel, I. F. 1996, *ARA&A*, 34, 749
- Saunders, W., Sutherland, W. J., Maddox, S. J., et al. 2000, *MNRAS*, 317, 55
- Schmidt, M., Schneider, D. P., & Gunn, J. E. 1995, *AJ*, 110, 68
- Schweitzer, M., Lutz, D., Sturm, E., et al. 2006, *ApJ*, 649, 79
- Scoville, N. Z., Frayer, D. T., Schinnerer, E., & Christopher, M. 2003, *ApJ*, 585, 105
- Solomon, P. M., Downes, D., & Radford, S. J. E. 1992, *ApJ*, 398, L25
- Solomon, P. M., Downes, D., Radford, S. J. E., & Barrett, J. W. 1997, *ApJ*, 478, 144
- Solomon, P. M., Vanden Bout, P. A. 2005, *ARA&A*, 43, 677
- Solomon, P., Vanden Bout, P., Carilli, C., & Guelin, M. 2003, *Nature*, 426, 636
- Staguhn, J. G., Schinnerer, E., Eckart, A., Scharwächter, J. 2004, *ApJ*, 609, 85
- Tacconi, L. J., Genzel, R., Lutz, D., et al. 2002, *ApJ*, 580, 73
- Tacconi, L. J., Genzel, R., Smail, I., et al. 2008, *ApJ*, 680, 246
- Tremaine, S., Gebhardt, K., Bender, R., et al. 2002, *ApJ*, 574, 740
- van der Werf, P. P., Isaak, K. G., Meijerink, R., et al. 2010, *A&A*, 518, L42
- Vestergaard, M. 2004, *ApJ*, 601, 676
- Wang, R., Carilli, C. L., Neri, R., et al. 2010, *ApJ*, 714, 699
- Walter, F., Riechers, D., Cox, P., et al. 2009, *Nature*, 457, 699
- Zheng, X. Z., Xia, X. Y., Mao, S., Wu, H., & Deng, Z. G. 2002, *AJ*, 124, 18
- Yun, M. S., Reddy, N. A., & Condon, J. J. 2001, *ApJ*, 554, 803

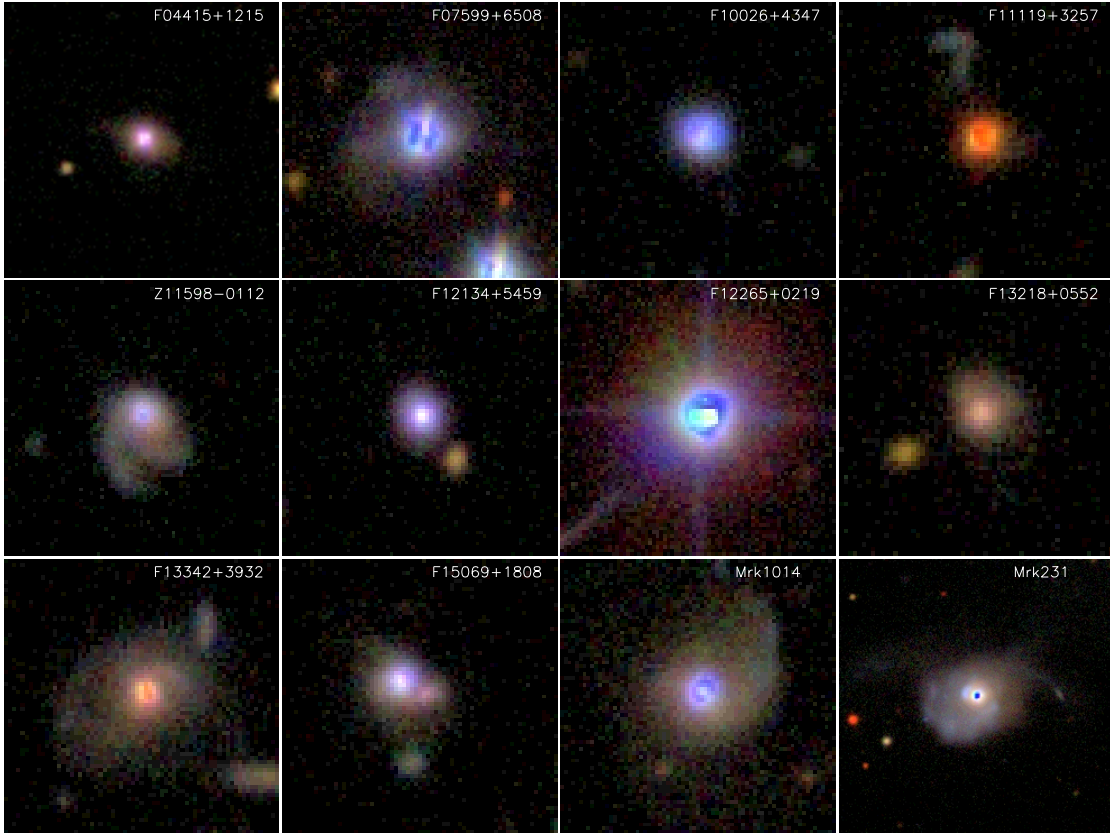


Fig. 1.— True color images of 12 IR QSOs (out of a total of 25), constructed from SDSS g, r, and i images using color-preserving nonlinear stretches (Lupton et al. 2004). The box size of each image is 80 kpc.

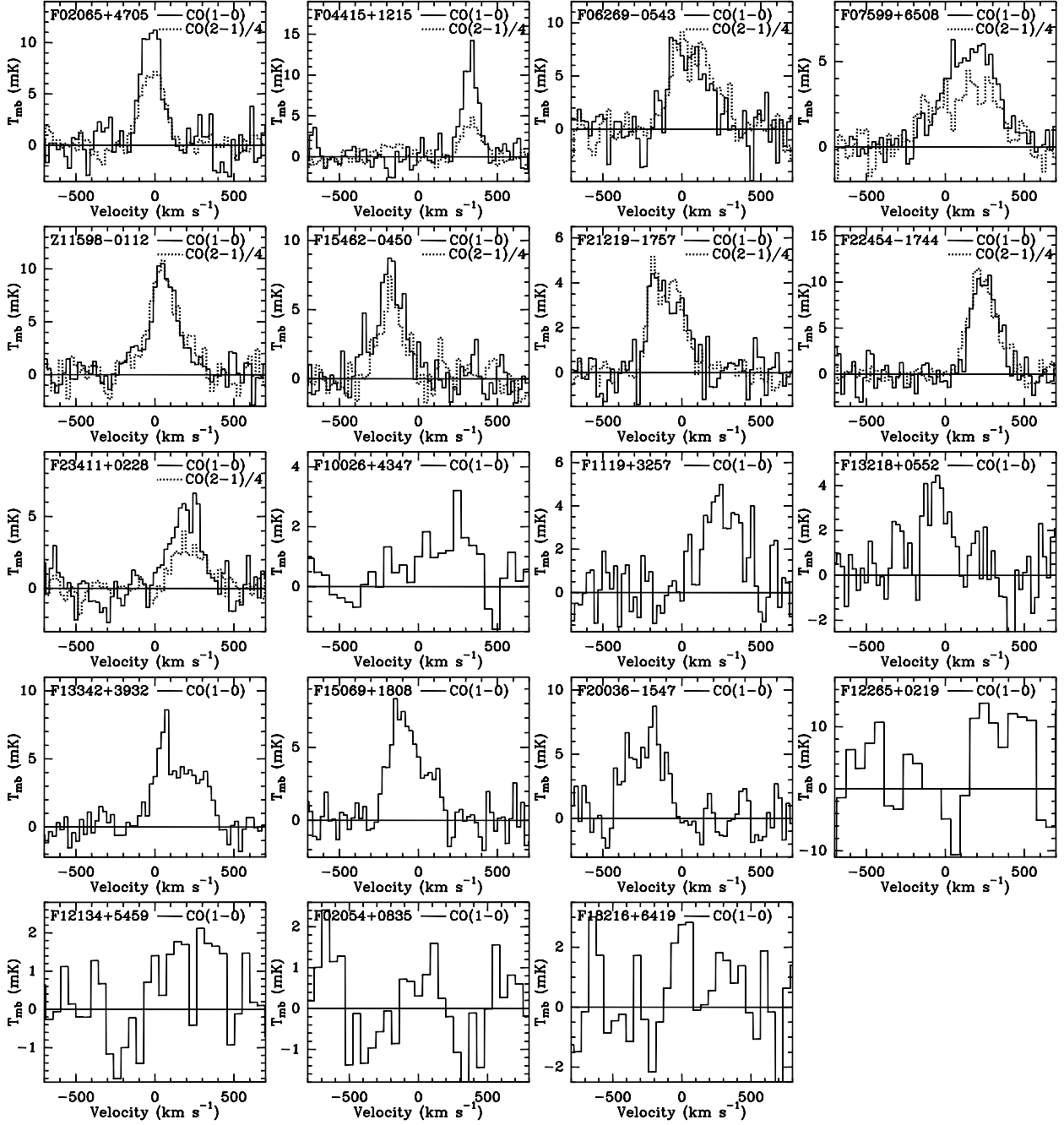


Fig. 2.— Spectra of CO (1-0) (solid lines) and CO (2-1) (dotted lines, divided by a factor of 4 for 9 targets) emission for our IR QSO sample. The spectra are smoothed to 23 km s<sup>-1</sup> channel width for display. Only marginal detections ( $3\sigma$ ) in F12265 and F12134, and non-detection in F02054 and F18216; for these objects, the spectra are smoothed to 46 km s<sup>-1</sup>. The main-beam temperature can be converted to the flux density using  $S/T_{\text{mb}}=4.95$  Jy/K.

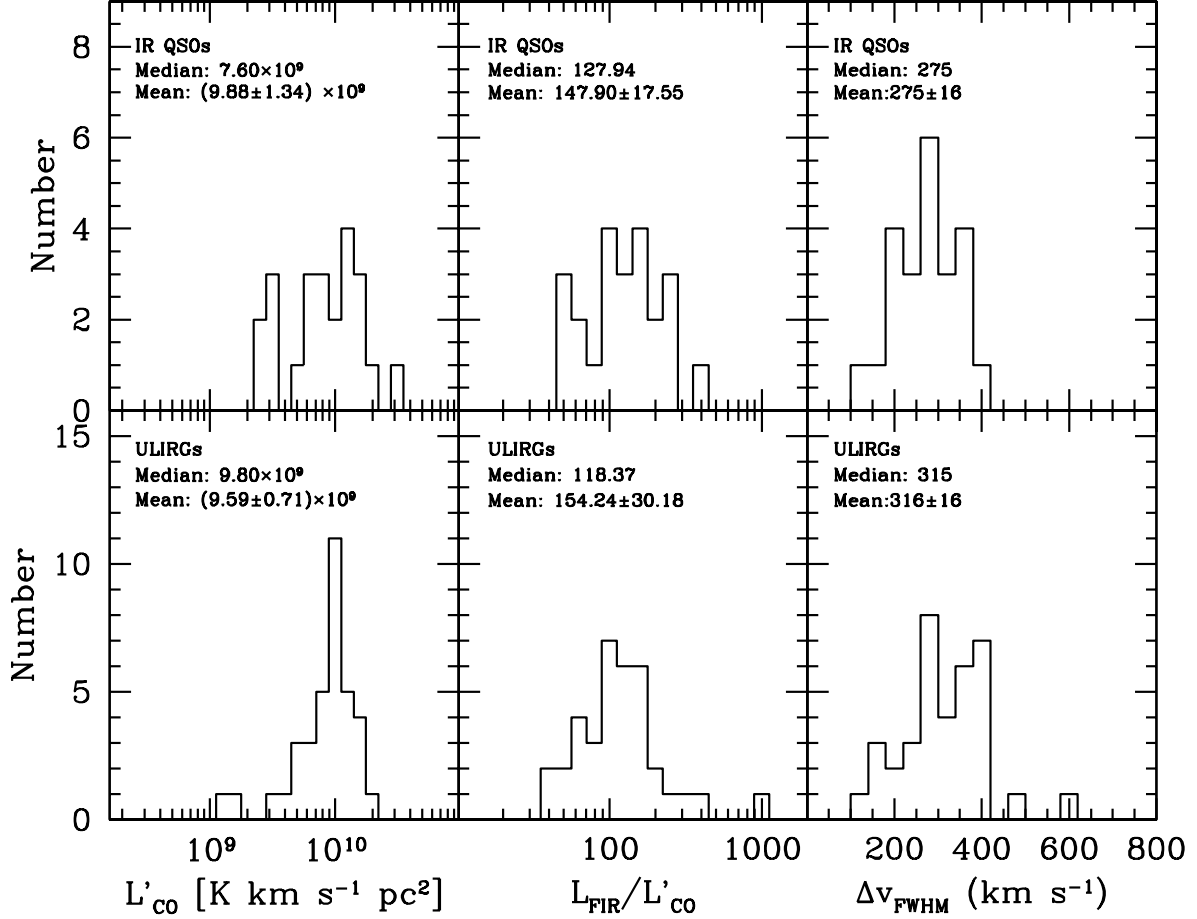


Fig. 3.— Histograms of CO (1-0) luminosity  $L'_{\text{CO}(1-0)}$ , star formation efficiency (ratio of far-infrared luminosity to CO luminosity)  $L_{\text{FIR}}/L'_{\text{CO}(1-0)}$  and CO line width (FWHM) for IR QSO hosts (upper panels) and ULIRGs (lower panels). The median and mean values are indicated in the top-left corner of each panel.

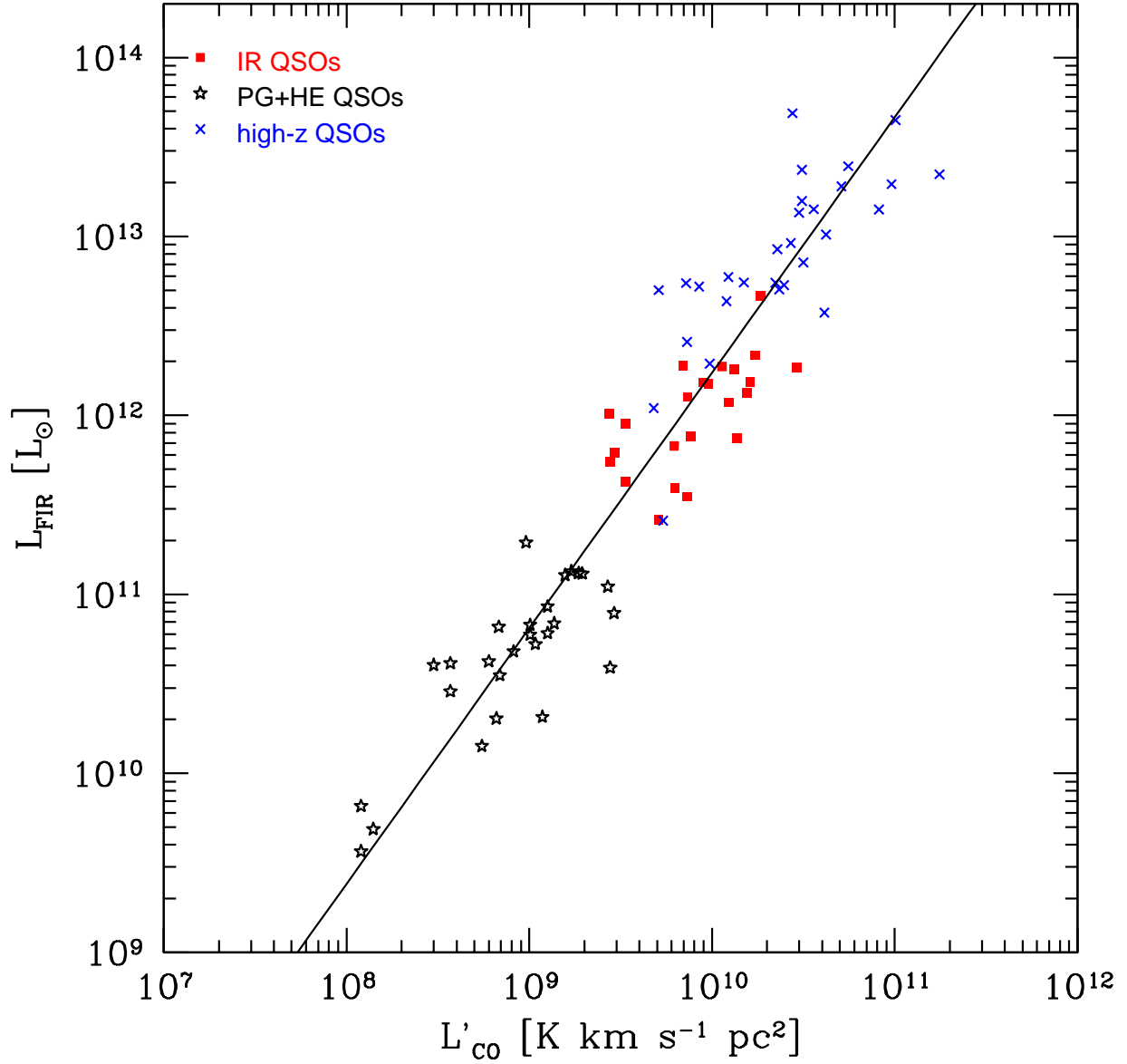


Fig. 4.—  $L_{\text{FIR}}$  vs.  $L'_{\text{CO}(1-0)}$  for almost all CO detected IR QSOs (red filled squares), PG+HE QSOs (black open pentagrams) and high-redshift QSOs (blue crosses). The samples are described in §2. A least-square bisector best-fit line obtained for all objects is shown; the best-fit power-law slope is  $1.4 \pm 0.1$ .

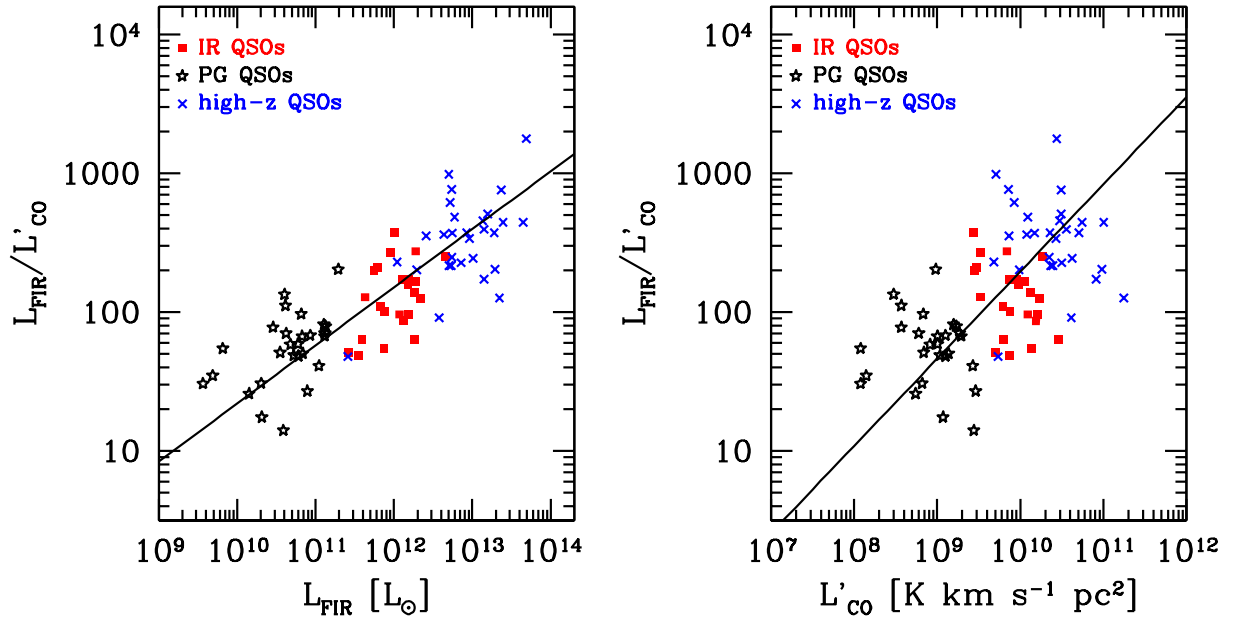


Fig. 5.— The star formation efficiency  $L_{\text{FIR}}/L'_{\text{CO}(1-0)}$  vs.  $L_{\text{FIR}}$  (left panel) and  $L_{\text{FIR}}/L'_{\text{CO}(1-0)}$  vs.  $L'_{\text{CO}(1-0)}$  (right panel) for three samples of QSOs (see §4.2). A Spearman Rank-order correlation analysis gives significances of  $> 99.99\%$  for both correlations. Notice that the vertical axis is independent of distance.

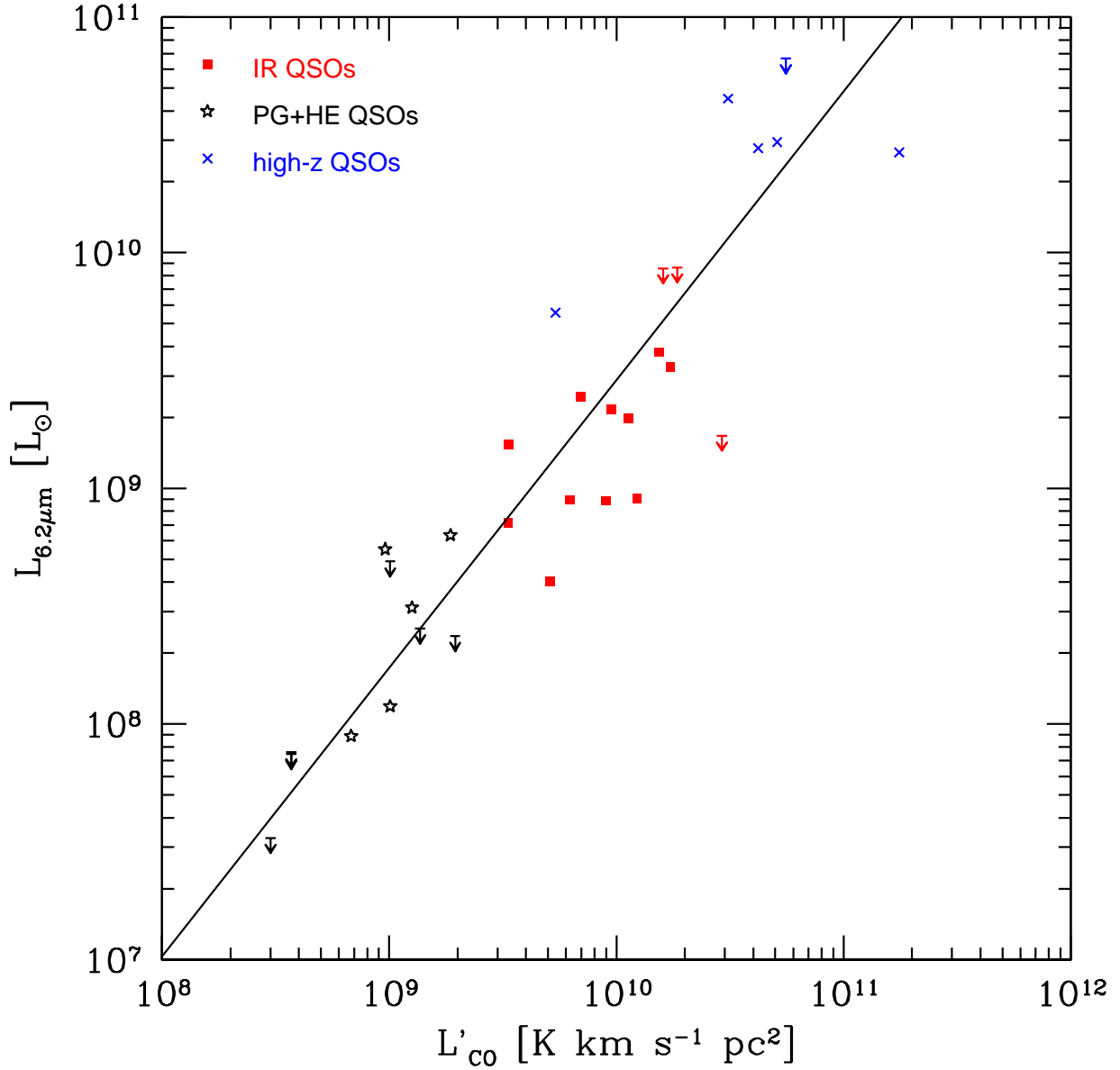


Fig. 6.— PAH  $6.2\mu\text{m}$  luminosity  $L_{6.2\mu\text{m}}$  vs.  $L'_{\text{CO}(1-0)}$  for PAH and CO detected IR QSOs, PG+HE QSOs and high-redshift QSOs. The PAH luminosities of low-redshift and high-redshift QSOs are taken from the Quasars and ULIRGs Evolution Study (see Schweitzer et al. 2006; Netzer et al. 2007) and Lutz et al. (2008) respectively, whereas PAH luminosities of IR QSOs are from Cao et al. (2008). Upper limits are plotted for some objects. A least-square bisector best-fit line is obtained for all objects, including those with upper limits.



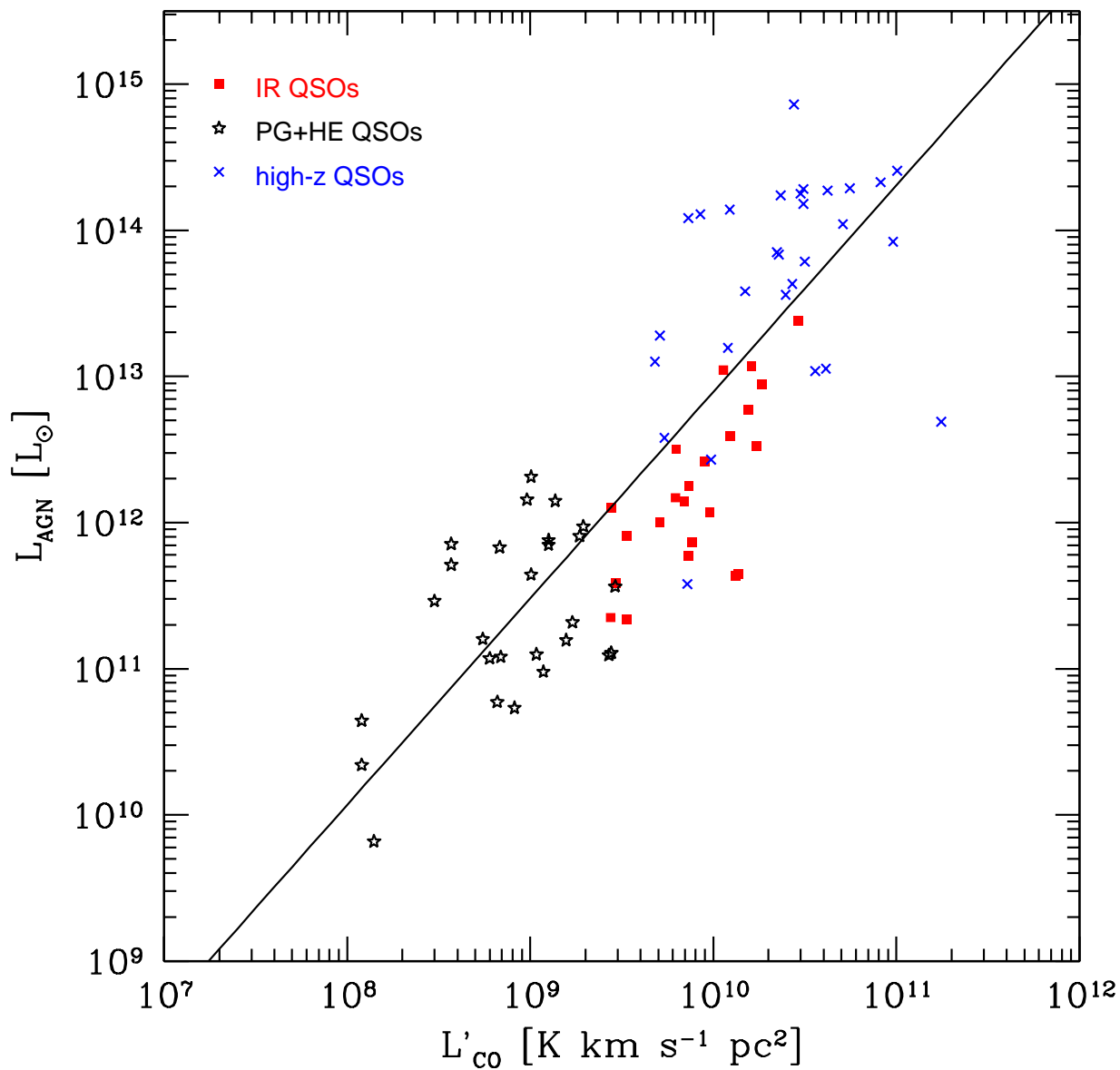


Fig. 7.— AGN-associated bolometric luminosity ( $L_{\text{AGN}}$ ) vs.  $L'_{\text{CO}(1-0)}$  for three samples of QSOs. A least-square bisector best-fit was performed for only low-redshift CO detected PG+HE QSOs; the best-fit power-law slope is  $1.4 \pm 0.2$ .

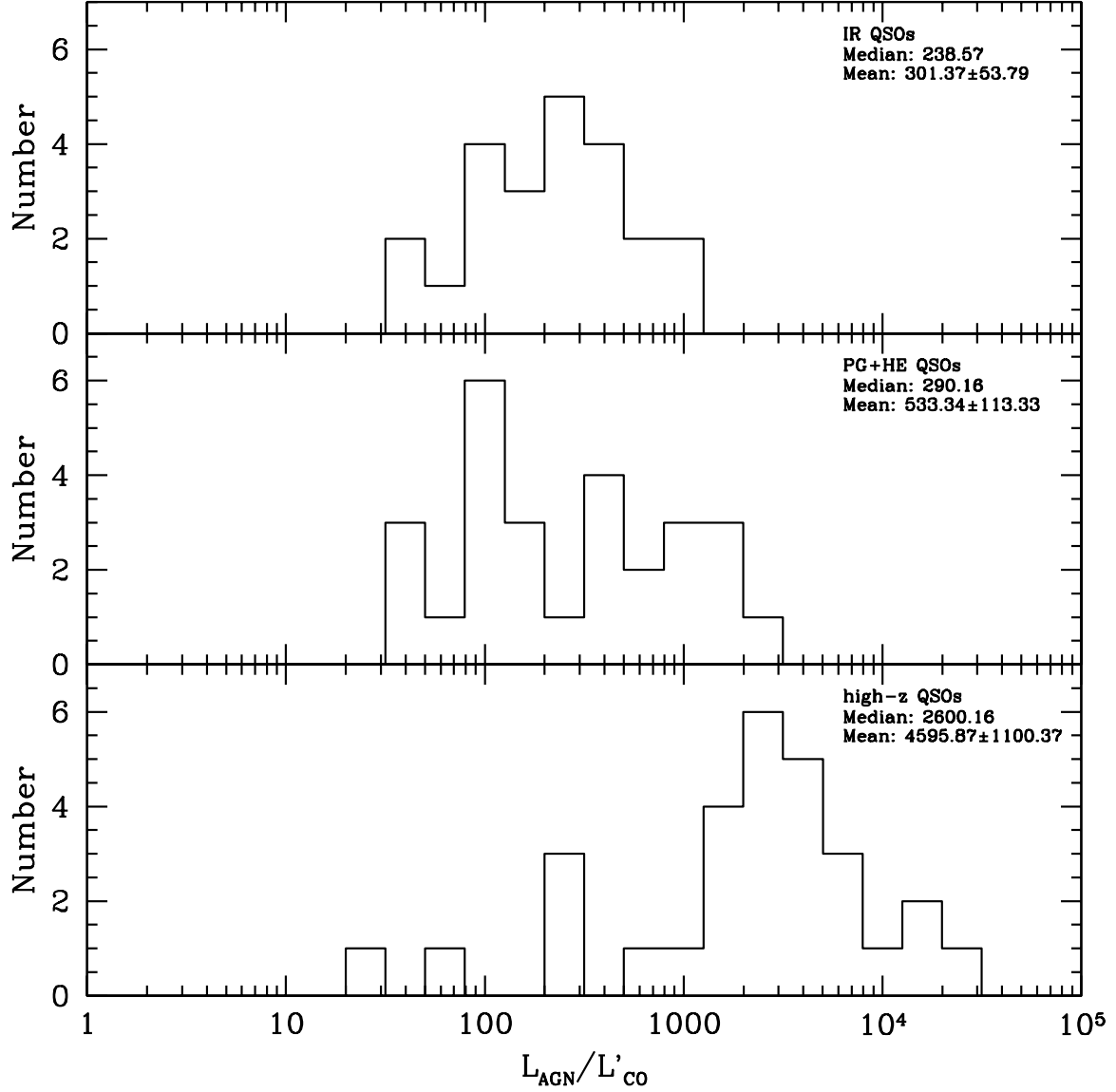


Fig. 8.— Histogram of the  $L_{\text{AGN}}$  to  $L'_{\text{CO}}$  ratio for IR QSOs (top panel), PG+HE QSOs (middle panel) and high-redshift QSOs (bottom panel). The median and mean values are indicated in the top right corner of each panel. Notice that a large fraction of optically bright PG QSOs are not detected in CO, thus the true median value of  $L_{\text{AGN}}/L'_{\text{CO}}$  taking into account the non-detections will be larger than that shown in the middle panel.

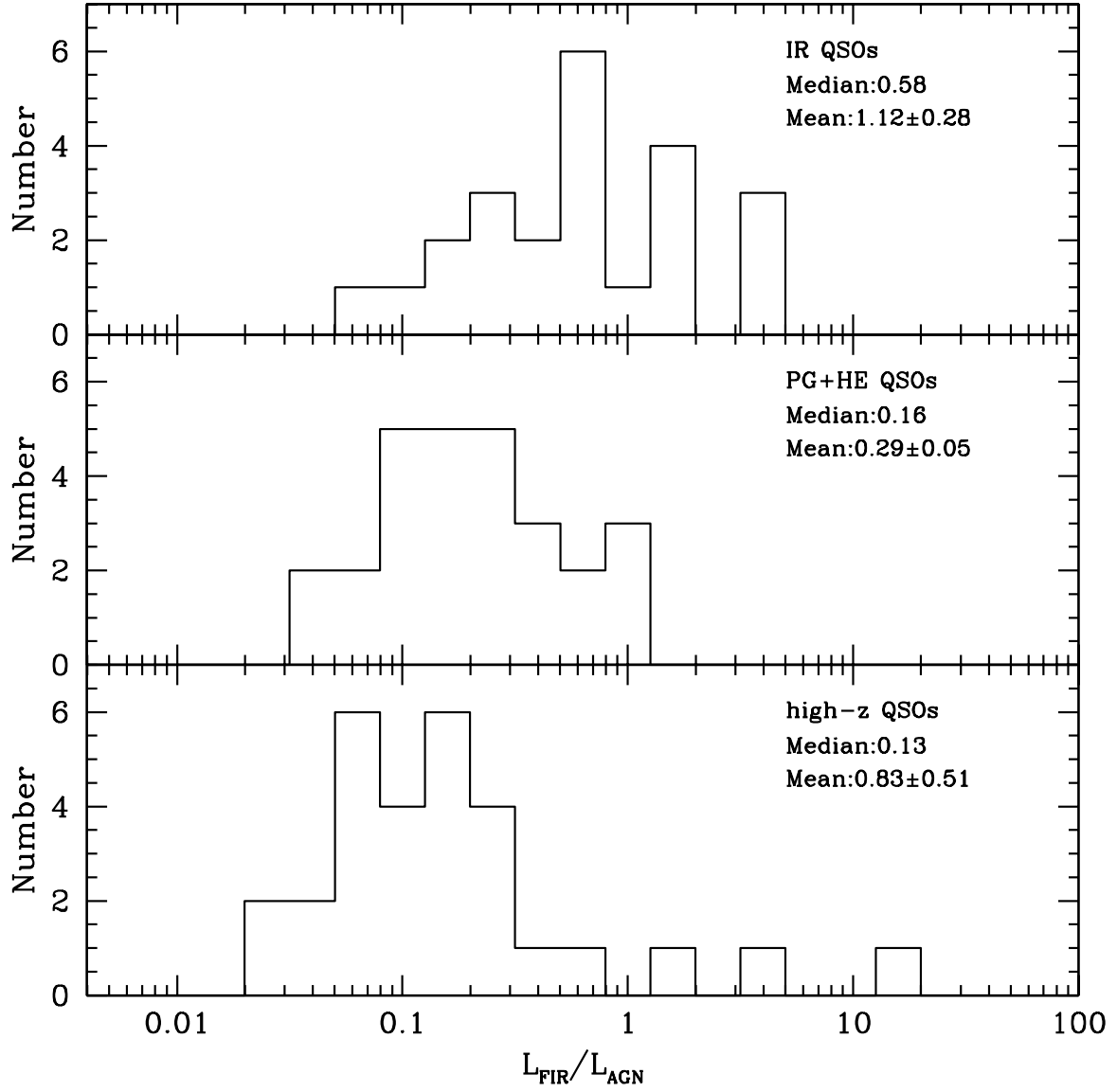


Fig. 9.— Histogram of  $L_{\text{FIR}}/L_{\text{AGN}}$  for IR QSOs (top panel), PG+HE QSOs (middle panel) and high-redshift QSOs (bottom panel). The median and mean values are indicated in the top right corner of each panel.

Table 1. CO observations of IR QSOs with the IRAM 30m telescope

Source	R.A. (J2000.0)	Decl. (J2000.0)	$z_{\text{opt}}$	$z_{\text{CO}}^a$	$D_{\text{L}}^b$ (Mpc)	Transition	$t_{\text{int}}^c$ (min)
Detections							
F02065+4705	02 09 45.8	+47 19 43.2	0.132	0.132	620	CO(1→0)	47
						CO(2→1)	47
F04415+1215	04 44 28.8	+12 21 13.1	0.089	0.090	407	CO(1→0)	85
						CO(2→1)	66
IR06269−0543	06 29 24.7	−05 45 26.0	0.117	0.117	545	CO(1→0)	97
						CO(2→1)	78
F07599+6508	08 04 30.4	+64 59 53.3	0.148	0.149	703	CO(1→0)	304
						CO(2→1)	219
F10026+4347	10 05 41.8	+43 32 41.6	0.178	0.179	861	CO(1→0)	99
F11119+3257	11 14 38.9	+32 41 33.0	0.189	0.190	920	CO(1→0)	94
Z11598−0112	12 02 26.6	−01 29 15.3	0.151	0.151	718	CO(1→0)	115
						CO(2→1)	72
F12265+0219	12 29 06.6	+02 03 09.0	0.158	0.159	755	CO(1→0)	150
F12134+5459	12 15 49.3	+54 42 24.6	0.150	0.151	713	CO(1→0)	140
F13218+0552	13 24 19.9	+05 37 05.0	0.205	0.204	1007	CO(1→0)	113
F13342+3932	13 36 24.0	+39 17 32.2	0.179	0.180	866	CO(1→0)	190
F15069+1808	15 09 13.7	+17 57 11.0	0.171	0.171	824	CO(1→0)	115
F15462−0450	15 48 56.8	−04 59 33.5	0.101	0.100	465	CO(1→0)	143
						CO(2→1)	91
F20036−1547	20 06 31.9	−15 39 05.8	0.193	0.192	942	CO(1→0)	98
F21219−1757	21 24 41.6	−17 44 45.3	0.113	0.113	525	CO(1→0)	198
						CO(2→1)	137
F22454−1744	22 48 04.1	−17 28 28.5	0.117	0.118	545	CO(1→0)	66
						CO(2→1)	66
F23411+0228	23 43 39.7	+02 45 05.7	0.091	0.092	416	CO(1→0)	113
						CO(2→1)	94
Non-detections							
F02054+0835	02 08 06.8	+08 50 05.2	0.345	...	1826	CO(1→0)	38
F18216+6419	18 21 57.3	+64 20 36.0	0.297	...	1535	CO(1→0)	58

Note. — Units of right ascension and declination are hours, minutes, seconds, and degrees, arcminutes, arcseconds respectively.

<sup>a</sup>CO redshift was determined by computing its flux-weighted redshift,  $z_{\text{CO}} = \sum I(z)z / \sum I(z)$  (see, e.g., Greve et al. 2005).

<sup>b</sup> $D_{\text{L}}$  is the luminosity distance.

<sup>c</sup>Total usable on-source integration time.

Table 2. CO emission line and infrared properties of the IR QSO sample

Source	Transition	$\Delta v_{\text{FWHM}}^a$ (km s <sup>-1</sup> )	$\Delta v_{\text{FWZI}}^b$ (km s <sup>-1</sup> )	$T_{\text{mb}}\Delta v^c$ (K km s <sup>-1</sup> )	$S_{\text{CO}}\Delta v^d$ (Jy km s <sup>-1</sup> )	$L'_{\text{CO}}^e$ (10 <sup>9</sup> K km s <sup>-1</sup> pc <sup>2</sup> )	$\log L_{\text{FIR}}$ (log L <sub>⊙</sub> )	$L_{\text{FIR}}/L'_{\text{CO}}$
Detections								
F02065+4705	CO(1→0)	145±12	300	1.84±0.17	9.11±0.84	7.60	11.885	101
	CO(2→1)	172±10	330	5.19±0.29	25.69±1.44	5.36		
F04415+1215	CO(1→0)	112±8	230	1.49±0.12	7.38±0.59	2.75	12.011	373
	CO(2→1)	137±16	280	2.48±0.29	12.28±1.44	1.14		
F06269-0543	CO(1→0)	258±25	465	2.28±0.22	11.29±1.09	7.36	12.103	172
	CO(2→1)	320±22	540	11.00±0.68	54.45±3.37	8.87		
F07599+6508	CO(1→0)	376±14	770	2.36±0.12	11.68±0.59	12.33	12.074	96
	CO(2→1)	486±44	840	7.36±0.78	36.43±3.86	9.60		
F10026+4347	CO(1→0)	343±92	580	0.81±0.16	4.01±0.79	6.20	11.830	109
F11119+3257	CO(1→0)	285±36	470	1.31±0.15	6.48±0.74	11.33	12.273	165
Z11598-0112	CO(1→0)	207±16	580	2.43±0.18	12.03±0.89	13.24	12.260	137
	CO(2→1)	234±18	580	9.71±0.70	48.06±3.46	13.19		
F12265+0219 <sup>f</sup>	CO(1→0)	313±86	480	4.88±1.41	24.16±6.98	29.11	12.266	63
F12134+5459 <sup>f</sup>	CO(1→0)	359±84	525	0.56±0.16	2.77±0.79	2.94	11.792	211
F13218+0552	CO(1→0)	299±64	430	0.93±0.18	4.60±0.89	9.51	12.175	157
F13342+3932	CO(1→0)	333±49	520	1.99±0.11	9.85±0.54	15.44	12.125	86
F15069+1808	CO(1→0)	287±50	440	1.95±0.14	9.65±0.69	13.71	11.875	55
F15462-0450	CO(1→0)	208±18	490	1.41±0.13	6.98±0.64	3.36	11.954	267
	CO(2→1)	177±18	370	4.25±0.32	21.04±1.58	2.54		
F20036-1547	CO(1→0)	263±23	420	1.91±0.18	9.45±0.89	17.20	12.338	127
F21219-1757	CO(1→0)	275±82	400	1.11±0.09	5.49±0.45	3.34	11.631	128
	CO(2→1)	243±28	380	4.19±0.19	20.74±0.94	3.14		
F22454-1744	CO(1→0)	186±13	380	2.27±0.19	11.23±0.94	7.31	11.548	48
	CO(2→1)	201±7	450	9.30±0.35	46.04±1.73	7.49		
F23411+0228	CO(1→0)	218±22	430	1.44±0.16	7.13±0.79	2.78	11.742	199
	CO(2→1)	229±21	390	2.98±0.30	14.75±1.48	1.43		
Non-detections								
F02054+0835	CO(1→0)	...	...	< 0.44	< 2.17	< 12.91	12.655	> 350
F18216+6419 <sup>g</sup>	CO(1→0)	...	...	< 0.70	< 3.46	< 15.08	12.694	> 328
Literature sources								
PG 0050+124 <sup>h</sup>	CO(1→0)	370	...	6.0±0.2	30±1.1	5.12	11.417	51
Mrk 1014 <sup>h</sup>	CO(1→0)	270	...	1.1±0.1	5.5±0.5	6.94	12.279	274
Mrk 231 <sup>i</sup>	CO(1→0)	230	...	22.0	99.0	8.98	12.185	171
PG 1613+658 <sup>h</sup>	CO(1→0)	400	...	1.6±0.1	8.0±0.6	6.23	11.595	63
3C48 <sup>j</sup>	CO(1→0)	330	...	...	1.9±0.2	18.49	12.666	251
PG1700+518 <sup>k</sup>	CO(1→0)	260	...	0.79±0.14	3.9±0.7	16.07	12.186	95

<sup>a</sup>The full width at half maximum (FWHM) obtained from Gaussian fit.

<sup>b</sup>The full width at zero intensity (FWZI) of the CO emission line width.

<sup>c</sup>The total CO line intensity  $I_{\text{CO}}$  obtained by integrating  $T_{\text{mb}}$  over the full velocity range, the errors were calculated using equation (1) in Matthews & Gao (2001).

<sup>d</sup> $S_{\text{CO}}\Delta v$  is the CO flux obtained using the conversion factor  $S/T_{\text{mb}}=4.95 \text{ JK}^{-1}$

<sup>e</sup> $L'_{\text{CO}} = 2.45 \times 10^3 \left( \frac{S_{\text{CO}}\Delta v}{\text{Jy km s}^{-1}} \right) \left( \frac{D_L}{\text{Mpc}} \right)^2 (J^{-2}(1+z)^{-1}) [\text{K km s}^{-1} \text{ pc}^2]$  (see, e.g., Solomon et al. 1997).

<sup>f</sup>Marginally detected with a signal-to-noise ratio of  $\sim 3$ .

<sup>g</sup>Aravena et al. (2011) report the CO (1-0) detection for PG1821+643 by CARMA. The detected CO(1-0) luminosity is about one half of the  $3\sigma$  upper limit shown here.

<sup>h</sup>Evans et al. (2006)

<sup>i</sup>Solomon et al. (1997); Kim & Sanders (1998)

<sup>j</sup>Krips et al. (2005); Heckman et al. (1992)

<sup>k</sup>Evans et al. (2009)

Table 3. Median values of physical parameters for IR QSOs, PG+HE QSOs and high-redshift QSOs

Name	$L_{\text{FIR}}$ ( $10^{12} L_{\odot}$ )	SFR ( $M_{\odot} \text{ yr}^{-1}$ )	$L_{\text{AGN}}$ ( $10^{12} L_{\odot}$ )	$\dot{M}$ ( $M_{\odot} \text{ yr}^{-1}$ )	$M_{\text{BH}}^a$ ( $10^7 M_{\odot}$ )	$M_{\text{gas}}^b$ ( $10^9 M_{\odot}$ )	$M_{\text{dyn}}^c$ ( $10^{11} M_{\odot}$ )
IR QSO	1.2	391	1.4	0.9	5	6	0.9
PG+HE QSO	0.05	16	0.2	0.13	20	0.8	2
high-redshift QSO	7	2300	100	70	200	20	2.1

Note. — The median values of parameters shown in this table are not obtained for all our sample objects due to incomplete information for some.

<sup>a</sup>The black hole masses for local IR QSOs and PG QSOs are from Hao et al. (2005); for high-redshift QSOs, the median value of black hole masses are taken from Coppin et al. (2008) for QSOs at  $z \sim 2$ . From the most recent measurement by De Rosa et al. (2011), the black hole masses for QSOs at  $4 < z < 6.5$  are  $\sim 10^9 M_{\odot}$ , smaller than those at lower redshift. Notice that the median value of the black hole masses for the local classical QSOs are only based on PG QSOs due to the lack of  $M_{\text{BH}}$  information for HE QSOs.

<sup>b</sup>The molecular gas mass for all QSOs is estimated from  $L'_{\text{CO}(1-0)}$  with a conversion factor of  $\alpha_{\text{CO}} = 0.8 M_{\odot} (\text{K km s}^{-1} \text{ pc}^2)^{-1}$ .

<sup>c</sup>The dynamical masses of IR QSOs and PG QSOs are from Dasyra et al. (2006, 2007). Notice that we assume the median value of dynamical mass for IR QSOs is the same as that of local ULIRGs. The dynamical masses for high-redshift QSOs are estimated by the median value of their CO line width (see Coppin et al. 2008).